DEVELOPMENT OF PHYSICAL PERFUSION PHANTOMS FOR X-RAY AND CT IMAGING: A PRACTICAL GUIDE

L.C. Goris[1,2], I. Sechopoulos[1,2,3]

[1] Technical Medical Center, University of Twente, Enschede, The Netherlands
[2] Department of Medical Imaging, Radboud University Medical Center, Nijmegen, The Netherlands
[3]Dutch Expert Centre for Screening (LRCB), Nijmegen, The Netherlands

Abstract— **Perfusion phantoms are increasingly used for developing and validating perfusion imaging techniques across modalities. However, the practical aspects of designing and implementing these phantoms are often underreported, which can lead to reproducibility challenges and hinder efficient progress. Improved documentation of these aspects can streamline future development and facilitate more rapid research progress. This paper provides a practical overview of perfusion phantom development particularly for X-ray imaging and computed tomography, outlining a step-by-step workflow and key technical and design considerations. These include microcirculation simulation, 3D printing methods, flow circuit configuration, and selection of working fluids and contrast agents to accurately mimic in vivo conditions. Strategies for mitigating air bubble formation are also discussed. This work serves as a reference for researchers seeking to design, construct, and validate reliable perfusion phantoms for quantitative imaging.**

Keywords— **Perfusion phantoms, perfusion imaging, computed tomography**

I. INTRODUCTION

Perfusion phantoms are essential tools for simulating tissue perfusion processes and vascular pathologies, providing a controlled and quantifiable ground truth for the optimisation, validation, and evaluation of medical imaging systems. Compared to *in vivo* studies, phantom-based studies offer a known ground truth, improved controllability and ethical feasibility [1,2].

In X-ray and computed tomography (CT) imaging, perfusion phantoms have been used to investigate dynamic contrast enhancement protocols and perfusion quantification accuracy [3-7]. As perfusion imaging becomes increasingly important for clinical diagnosis and treatment planning, with applications in fields such as oncology, stroke, and cardiovascular imaging, the need for standardised and reproducible phantoms continues to grow.

In earlier work, we introduced a framework for phantom development based on the design science research methodology (DSRM), providing a structured approach to the iterative design and evaluation of imaging phantoms [3]. Building upon that foundation, this paper focuses on providing a guide on practical implementation aspects that should be considered in perfusion phantom development.

When developing perfusion phantoms, several technical considerations arise. These include selecting appropriate construction materials and choosing fabrication techniques such as 3D printing or mould casting to accurately simulate macro- and microcirculation. In addition, the flow circuit must be designed to reproduce physiologically relevant flow profiles. Furthermore, the working fluid and contrast agents should be selected to ensure realistic fluid dynamics in replicating *in vivo* conditions. Additional challenges, such as preventing and removing air bubbles, require effective mitigation strategies.

This paper presents a practical guide to perfusion phantom development, revisiting the phantom development framework and outlining key technical and design considerations to support the development of reproducible, physiologically relevant, and imaging-compatible perfusion phantoms.

II. PERFUSION IMAGING AND X-RAY CONTRAST AGENTS

Perfusion imaging aims to quantify blood flow through the microvasculature of tissues. The microcirculation represents the terminal vascular network, comprising of arterioles, capillaries, and venules, with vessel diameters below 20 μm [8]. It is responsible for delivering oxygen and nutrients to parenchymal cells and maintaining tissue metabolism.[8] Disturbances in microcirculatory flow are central to many diseases: reduced cerebral perfusion is critical in stroke assessment, [9] and increased perfusion and angiogenesis are hallmarks of tumour growth and malignancy.[10] Quantifying these microvascular changes through perfusion imaging provides valuable biomarkers for diagnosis, treatment monitoring and prognosis[10].

In CT perfusion (CTP) imaging, an iodinated contrast agent is administered intravascularly and is monitored during its initial circulation through the tissue capillary bed of the organ of interest [11]. Iodinated contrast agents cause greater absorption of X-ray attenuation in a target organ or blood plasma, resulting in increased enhancement on the CT image. The extent of contrast enhancement in CT correlates directly with the iodine concentration in the system and the X-ray energy level. At a fixed tube voltage, contrast enhancement rises proportionally with iodine concentration [12]. Lower voltages result in greater contrast enhancement per iodine concentration since the lower effective energy of the X-ray beam is closer to the k-edge of iodine (33.2 keV) [13].

Theoretically, a 1 mg I/mL increase in concentration yields a contrast enhancement of 41.12 HU at 80 kV, 31.74 HU at 100 kV, and 26.18 HU at 120 kV. Therefore, a lower voltage produces greater contrast enhancement per iodine concentration [12].

After peripheral intravenous injection, the contrast bolus passes through the right atrium, pulmonary circulation, and left atrium before entering the central arterial system. It redistributes from the vascular to the interstitial space, with transport governed mainly by blood flow rather than diffusion. Consequently, highly perfused organs such as the kidneys, spleen, and liver demonstrate strong first-pass enhancement. As the bolus circulates, it becomes progressively diluted and dispersed, particularly in organs located further from the injection site [12]. Typically, the contrast protocol for a brain perfusion CT uses 35-50 mL of an iodinated contrast agent with a concentration of 300-350 mg I/mL (injected rapidly), and the derived iodine maps in the brain report parenchymal iodine concentrations in the order of 0.4-8.6 mg I/mL, depending on the timing and pathology [14], [15]. Contrast-enhanced CT images of the breast reveal maximum iodine concentrations up to 6 mg I/mL in cancerous tissue [16].

The changes in tissue contrast per voxel over time can be used to compute time-intensity curves. From these curves, parameters such as time to peak (TTP), mean transit time (MTT), maximum slope, time of arrival, area under the curve, and peak intensity can be extracted. Colour-coded parametric maps can also be generated to help visualise these tissue characteristics [17]. Blood Volume (BV), which refers to the amount of blood per mass of tissue, and Blood Flow (BF), which is the amount of blood per mass of tissue per minute, can be calculated using the contrast enhancement of the arterial input, tissue, and venous outflow [11].

III. PHANTOM DEVELOPMENT WORKFLOW

To provide structure to perfusion phantom development, we previously proposed a workflow consisting of six iterative steps: (1) identifying the problem (2) defining objectives for a solution; (3) designing and developing the phantom; (4) demonstrating its functionality; (5) evaluating its performance against the predefined objectives; and (6) communicating the results. These steps are represented in a V-shaped model (Figure 1), distinguishing a verification, where user needs, functional requirements, and physical design are defined and realised, from a validation phase, where the phantom's performance is tested against its intended purpose [3].

IV. KEY TECHNICAL AND DESIGN CONSIDERATIONS

Once the functional and design requirements are established, the phantom can be designed. This section covers the key design and technical considerations for X-ray/CT perfusion phantoms, including possible materials for simulating microcirculation, pump system design and flow profiles, contrast agents and fluid properties, flow sensors, and methods to eliminate air bubbles inside the setup.

Simulating Microvasculature

The material used to simulate microvasculature should match the X-ray attenuation properties of the target tissue, typically corresponding to a Hounsfield Unit (HU) range of approximately 50 HU to 80 HU.[18] Flow dynamics within the simulated microvasculature should reproduce the enhancement patterns observed *in vivo* for the tissue of interest, ensuring realistic time-intensity characteristics. The material used to simulate the microcirculation should not

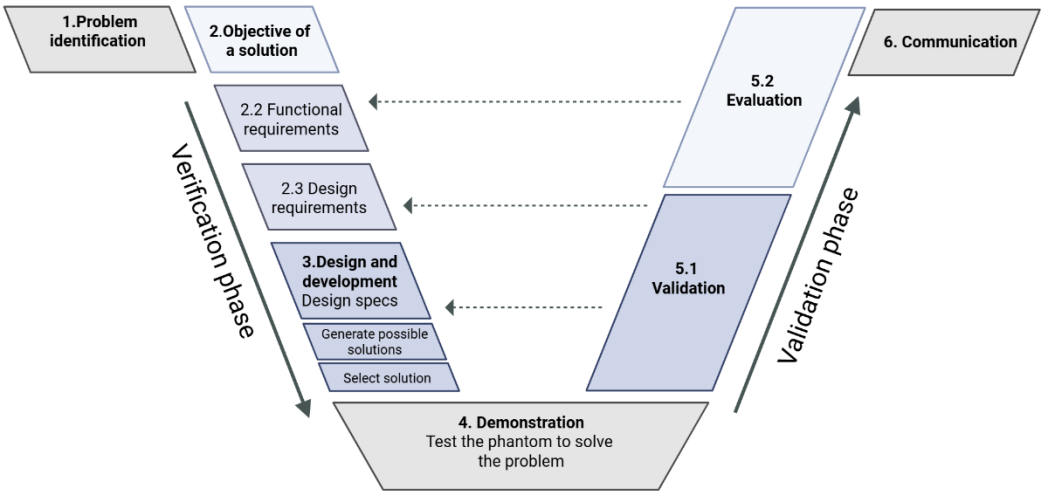

Figure 1: Visual representation of the phantom development workflow. The workflow is shown as a V-shaped model that separates a verification phase (where the requirements are established and the phantom is designed) from a validation phase (where the phantom is tested against its requirements and its performance is tested).

contain any air bubbles, as these can introduce imaging artefacts and alter local X-ray attenuation measurements.

Kamphuis et al. conducted a systematic review categorising perfusion phantom designs into three main configurations: basic, aligned capillary, and tissue-filled [1]. Basic designs comprise a single chamber with inlet and outlet tubing, without attempting to replicate the physiological or morphological structure of the microcirculation or surrounding tissue. In aligned capillary phantoms, the microvascular network is modelled using a bundle of parallel hollow fibres or tubes, such as those found in dialysis cartridges, to represent capillary pathways [19]. Tissue-filled phantoms incorporate tissue-mimicking materials within the phantom volume to better approximate microcirculatory architecture.

Table 1: Microcirculation simulation materials, example uses, and their advantages and disadvantages

Material	Example application	Advantages	Disadvantages/ limitations
Sponge-like polymer	*MRI*[20], [21], [22], [23] *US*[24] *CT*[6]	Inexpensive, high porosity, compressible	Limited repeatability, Variable pore size Air entrapment
(micro) beads	*MRI*: dextran gel beads (porous)[25] *CT*: Sodium alginate beads (non-porous)[3], POM beads[4], Plastic beads[5] *PET/SPECT*: plastic beads[26] *Fluorescence angiography*: glass beads[27]	Compressible (gel beads) Repeatable Controlled pore geometry Tissue-like attenuation coefficients	Difficult integration in complex volumes Attenuation coefficient too high (glass beads)
Gel	*US*: Agar Bacto gel[28] *MRI*: Sephadex gel[29], 3D printing gel[30], gelatin and Joncryl[31]	Inexpensive customizable geometry	Limited mechanical durability Challenging to simulate small channels
3D-printed microchannels	*X-ray*: gyroid structure[32] *MRI*: microchannels [33] *CT*: Hexagonal channels[7], gyroid structure and small channels[34]	High design precision Rapid prototyping	Limited in the smallest channel size possible

Additionally, microvasculature simulation can be achieved either as a single continuous volume or as two distinct compartments separated by a porous membrane [1], [35]. Examples of tissue-mimicking materials include sponge-like materials [6], [20-24] (micro) beads [3-5], [25,26] gels [28-31] and 3D-printed microchannels [7], [32-34], [36]. Table 1 lists a summary of the potential materials along with their advantages and disadvantages for use in X-ray/CT perfusion imaging.

3D printing for perfusion phantoms

3D printing is increasingly used in medical imaging. It provides significant advantages such as customisation, rapid prototyping, reproducibility, high precision, and relatively low cost. For phantom development, 3D printing can therefore be a viable option [18], [37]. The field of 3D printing is advancing, allowing for printing with ever-higher resolutions and smaller channel sizes. This is especially relevant for perfusion phantoms, where small channels or complex vascular structures resembling macro and microvascular perfusion need to be simulated. Various printing techniques exist, including fused deposit modelling (FDM), vat photopolymerization (which includes stereolithography (SLA)), binder jetting, material jetting, powder bed fusion, directed energy deposition, and sheet lamination [38]. The most widely used methods are FDM and SLA printing. This section describes these two different techniques, material options, and phantom assembly strategies.

Fused Deposit Modelling

In FDM printing, a thermoplastic filament is fed into a temperature-controlled head, where it melts and is precisely extruded through a nozzle onto the print bed. As the material cools, it solidifies. After each layer, the nozzle moves upward to add the next layer. For overhanging structures, temporary support structures are often printed from additional filament that can be removed afterwards. The typical feature resolution of FDM prints is 100-150 microns[39]. FDM printing allows for inexpensive prints from materials with varying mechanical properties. FDM printers are widely accessible and used for prototyping, as well as for end-use manufacturing. Typical materials used for the filaments include: polylactic acid (PLA), acrylonitrile-butadiene-styrene (ABS), polymethyl methacrylate (PMMA), nylon, and polycarbonate (PC). These different materials have different X-ray attenuation values [18]. Okkalidis *et al.* (2024) and Ma *et al.* investigated the X-ray attenuation of thermoplastic filaments for X-ray/CT phantoms and identified proper filaments for simulating muscle, fat tissue, and bone [18], [40].

Vat photopolymerization

Vat photopolymerization is an additive manufacturing technique in which a photosensitive resin is selectively cured layer by layer using a light source, typically a laser (stereolithography, SLA) or a digital light projector (digital light processing, DLP), or through continuous liquid interface production (CLIP). After printing, the object undergoes post-processing steps, including washing with solvents to remove excess resin, removing possible

supporting structures, and subsequent ultraviolet curing to improve mechanical stability. A wide variety of materials can be employed in this process, such as clear, tough, flexible, or elastic resins, allowing fabrication to be tailored to specific functional and mechanical requirements. Vat photopolymerization allows for prints with excellent surface quality and precision (typical feature resolution of 50-100 microns) [41].

Phantom Assembly Strategies

A crucial requirement for perfusion phantoms is that the (assembled) print is watertight. The choice of printing material can play a key role in this. Resins used in SLA printing typically create water-tight parts, whereas for plastics used in FDM printing, it depends on printing quality and material properties. In the latter, epoxy resin, silicon or acrylic coatings can be applied post-printing to seal any leaks and guarantee water tightness [42,43].

When a phantom consists of multiple parts, thin silicon packing can be used between the parts, and the phantom can be tightened with nylon screws and bolts to create a seal [3].

Flow Set-ups

To create time-varying contrast profiles inside the phantom, a pumping system is required. Blood flow can be simulated using a continuous pump, while contrast agents can be administered using (programmable) syringe pumps or medical injectors. Care should be taken to prevent pressure drops caused by the continuous pump during contrast injection, as these can affect flow profiles. This can be achieved in several different ways. First, the continuous pump can be programmed to modify the speed during injection. Another option is to use an additional injecting pump that introduces water at the same rate as the contrast injection when contrast is not being administered. Finally, the contrast can be added to the input vessel from which the continuous pump draws the fluid.

The flow setup of the phantom can be either an open, a semi-closed or a closed system. Where an open system typically consists of an input tank, pump, contrast injection side, the phantom, and an output tank, a closed system combines or redirects the output with the input, thereby lowering the chances of introducing new air bubbles into the system. In the study by Kamphuis *et al.* a closed system was used with a custom-built filter to extract the radioactive material before re-entering the input reservoir [26]. Boese et al, created a semi-closed system by incorporating a tap for contrast removal after circulation through their phantom [6]. Different configurations are shown in Figure 2.

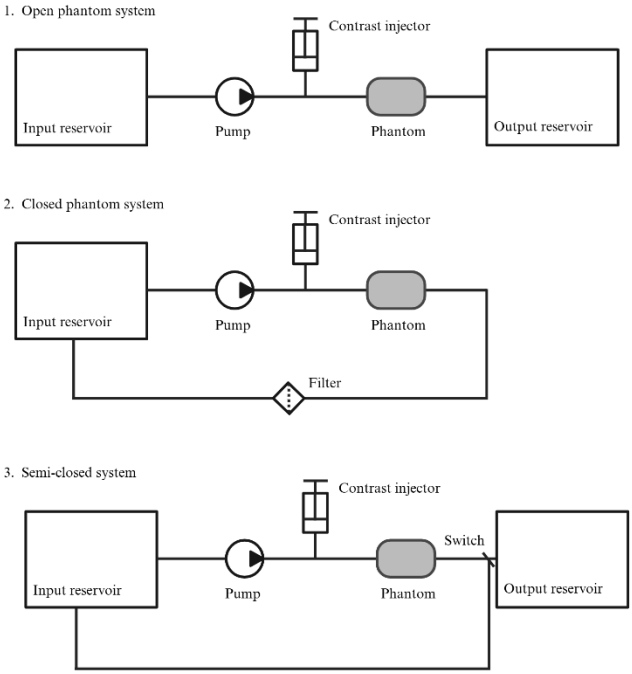

Figure 2: Phantom set-up configurations. Distinguishing open, closed and semi-closed phantom systems.

Contrast Agents and Fluid Properties

In perfusion phantoms, the distance from the injection site to the tissue compartment is generally much smaller and encompasses a smaller volume than its human equivalent. Therefore, the initial input concentration should be decreased to simulate the correct iodine concentrations expected to arrive at the area of the body being imaged. The required concentration can be estimated by taking the following steps [44]:

1. Determining the desired peak CT number HU_{target} and the base intensity of the phantom background HU_{base}.
2. Measuring the scanner slope S (HU per mg I/mL) at the desired scanner settings by measuring a calibration series of known iodine concentrations and fitting HU vs iodine concentration to obtain S.
3. Determining the required iodine concentration in the imaged volume (after dilution/mixing):

$$[I]_{imaged}(mg\ I/\ mL) = \frac{HU_{target} - HU_{base}}{S} \quad (1)$$

4. Relating the injected contrast to the imaged concentration, while accounting for dilution.
5. When the injected bolus $V_{inj}(mL)$ and iodine contrast agent with a certain concentration C_{agent} (mg I/mL) mixes into an effective dispersion volume $V_{disp}(mL)$ in the phantom or flow loop, then:

$$[I]_{imaged} \approx \frac{V_{inj} \cdot C_{agent}}{V_{disp}} \quad (2)$$

So:

$$V_{inj} = \frac{[I]_{imaged} \cdot V_{disp}}{C_{agent}} \quad (3)$$

6. When the phantom transit is nearly plug-flow with little dilution, V_{disp} approximates V_{inj}. The dispersion of the contrast agent inside the flow loop and the phantom should be studied beforehand.
7. Determining the iodine delivery rate (IDR), by taking the injection flow rate (FR) into account:

$$IDR\ (mg\ I/\ s) = C_{agent}(mg\ I/\ mL) \cdot FR\ (mL/\ s) \quad (4)$$

Studying Contrast Agent Behaviour

Viscous fluids generally have more resistance and flow more slowly when combined with a less viscous counterpart [45]. As a result, care must be taken when attempting to use iodinated contrast agents mixed with water in a perfusion phantom, since the former have a higher dynamic viscosity than the latter. In addition, the higher the iodine concentration, the higher the viscosity. For example, Iomeron 400 has a dynamic viscosity of 12.6 cP at 37 degrees Celsius [46], while blood has a viscosity of 3.5-5.5 cP at this temperature. However, it should be noted that blood viscosity changes depending on the hemodynamic conditions [47]. Mismatch in viscosity between the contrast agent and the underlying base fluid, e.g., water, will result in poor contrast integration and transport, failing to represent the clinical conditions. To minimise this problem, matching the dynamic properties, in terms of density and viscosity, between the contrast and the base fluid is essential. This can be achieved by, e.g., including glycerol together with water as the base fluid [48] and by diluting the contrast agent to match the properties of the analogue agent at the imaged site.

For example, in an early functional imaging study performed to evaluate imaging of the lymphatic vessel, it was determined that better contrast integration was observed when the dynamic properties of the iodinated contrast agent and the lymphatic fluid analogue matched [49] This was achieved by diluting Iomeron 56 to match the analogue blood-mimicking fluid (BMF), consisting of 45 wt% glycerol and 55 wt% water [48]. In general, it is useful for studying contrast agent behaviour in perfusion phantoms to add a few drops of food colouring to the contrast agent.

A. Overcoming Air Bubbles

Air bubbles within a phantom setup represent a significant source of error since the density difference between air (approximately -1000 HU) and water- or tissue-equivalent material (0-80 HU) creates discontinuities in X-ray attenuation that do not reflect actual tissue structure [18] compromising quantitative, and sometimes qualitative, evaluations. To overcome air bubbles in the phantom setup, several strategies can be employed during phantom preparation. Degassing the water or BMF before use reduces the likelihood of trapped microbubbles. Flushing the phantom repeatedly and filling it from bottom to top helps displace residual air. Gently shaking or tilting the phantom during filling can release trapped bubbles. Furthermore, it is essential to ensure that the phantom is completely watertight and does not allow air bubbles to enter through small gaps.

Flow Sensors and Ground Truth Values

Flow sensors can be used to provide real-time, quantitative ground-truth flow values of the phantom. Various types of sensors can be employed for this purpose, including Doppler-based flow sensors, which measure velocity through frequency shifts of reflected ultrasound or laser signals, and turbine flow sensors, which determine flow rates from the rotational speed of an internal rotor [26]. Flow regulation typically depends on adjusting the pump speed and manually tuning resistive elements, such as taps, to achieve the desired flow conditions. While this approach enables control, it relies on continuous monitoring and manual intervention. Once flow conditions have been established, the flow sensor readings often remain stable, reducing the necessity for continuous monitoring. To further streamline the process, the use of pre-calibrated flow resistors (apertures) within a standardised configuration has been proposed. Such an approach could simplify the setup and improve user friendliness [50].

V. CONCLUSIONS

Developing a reliable perfusion phantom requires careful consideration of both design principles and practical implementation. We outlined a step-by-step approach from the initial design workflow and microcirculation simulation to fabrication using 3D printing methods. Attention to watertight sealing, realistic flow generation, and physiologically relevant fluid properties is essential to achieve consistent and meaningful results. Addressing common challenges, such as air bubble formation, further ensures accurate flow quantification. By combining accessible materials with reproducible fabrication and structured validation, researchers can create perfusion phantoms optimised for their specific imaging needs.

REFERENCES

[1] M. E. Kamphuis, M. J. W. Greuter, R. H. J. A. Slart, and C. H. Slump, “Quantitative imaging: systematic review of perfusion/flow phantoms,” *Eur. Radiol. Exp.*, vol. 4, no. 1, p. 15, Mar. 2020, doi: 10.1186/s41747-019-0133-2.

[2] S. Manohar, I. Sechopoulos, M. Anastasio, L. Maier-Hein, and R. Gupta, “Super phantoms: advanced models for testing medical imaging technologies,” *Commun. Eng.*, vol. 3, May 2024, doi: 10.1038/s44172-024-00218-z.

[3] L. C. Goris, A. H. A. Z. Al-Kaylani, R. C. L. Schuurmann, M. J. W. Greuter, R. P. H. Bokkers, and S. Manohar, “Development of a

cerebral CT perfusion phantom: A structured approach," *Phys. Medica Eur. J. Med. Phys.*, vol. 131, Mar. 2025, doi: 10.1016/j.ejmp.2025.104944.

[4] C. Mathys *et al.*, "A Phantom Approach to Interscanner Comparability of Computed Tomographic Brain Perfusion Parameters," *J. Comput. Assist. Tomogr.*, vol. 36, no. 6, p. 732, Dec. 2012, doi: 10.1097/RCT.0b013e31826801df.

[5] B. P. Ziemer, L. Hubbard, J. Lipinski, and S. Molloi, "Dynamic CT perfusion measurement in a cardiac phantom," *Int. J. Cardiovasc. Imaging*, vol. 31, no. 7, pp. 1451–1459, Oct. 2015, doi: 10.1007/s10554-015-0700-4.

[6] A. Boese *et al.*, "Performance evaluation of a C-Arm CT perfusion phantom," *Int. J. Comput. Assist. Radiol. Surg.*, vol. 8, no. 5, pp. 799–807, Sept. 2013, doi: 10.1007/s11548-012-0804-4.

[7] L. Low, S. Ramadan, C. Coolens, and H. E. Naguib, "3D printing complex lattice structures for permeable liver phantom fabrication," *Bioprinting*, vol. 10, p. e00025, June 2018, doi: 10.1016/j.bprint.2018.e00025.

[8] G. Guven, M. P. Hilty, and C. Ince, "Microcirculation: Physiology, Pathophysiology, and Clinical Application," *Blood Purif.*, vol. 49, no. 1–2, pp. 143–150, Feb. 2020, doi: 10.1159/000503775.

[9] A. Bivard, N. Spratt, C. Levi, and M. Parsons, "Perfusion computer tomography: imaging and clinical validation in acute ischaemic stroke," *Brain*, vol. 134, no. 11, pp. 3408–3416, Nov. 2011, doi: 10.1093/brain/awr257.

[10] R. Lugano, M. Ramachandran, and A. Dimberg, "Tumor angiogenesis: causes, consequences, challenges and opportunities," *Cell. Mol. Life Sci. CMLS*, vol. 77, no. 9, pp. 1745–1770, Nov. 2019, doi: 10.1007/s00018-019-03351-7.

[11] A. A. Konstas, G. V. Goldmakher, T.-Y. Lee, and M. H. Lev, "Theoretic basis and technical implementations of CT perfusion in acute ischemic stroke, part 1: Theoretic basis," *AJNR Am. J. Neuroradiol.*, vol. 30, no. 4, pp. 662–668, Apr. 2009, doi: 10.3174/ajnr.A1487.

[12] K. T. Bae, "Intravenous Contrast Medium Administration and Scan Timing at CT: Considerations and Approaches," *Radiology*, vol. 256, no. 1, pp. 32–61, July 2010, doi: 10.1148/radiol.10090908.

[13] S. P. Kalva, D. V. Sahani, P. F. Hahn, and S. Saini, "Using the K-edge to Improve Contrast Conspicuity and to Lower Radiation Dose With a 16-MDCT: a Phantom and Human Study," *J. Comput. Assist. Tomogr.*, vol. 30, no. 3, p. 391, June 2006.

[14] D. Byrne *et al.*, "Prediction of Hemorrhage after Successful Recanalization in Patients with Acute Ischemic Stroke: Improved Risk Stratification Using Dual-Energy CT Parenchymal Iodine Concentration Ratio Relative to the Superior Sagittal Sinus," *Am. J. Neuroradiol.*, vol. 41, no. 1, pp. 64–70, Jan. 2020, doi: 10.3174/ajnr.A6345.

[15] U. K. Bodanapally, K. Shanmuganathan, Y. P. Gunjan, G. Schwartzbauer, R. Kondaveti, and T. R. Feiter, "Quantification of Iodine Leakage on Dual-Energy CT as a Marker of Blood-Brain Barrier Permeability in Traumatic Hemorrhagic Contusions: Prediction of Surgical Intervention for Intracranial Pressure Management," *Am. J. Neuroradiol.*, vol. 40, no. 12, pp. 2059–2065, Dec. 2019, doi: 10.3174/ajnr.A6316.

[16] F. C. Hasse *et al.*, "Improvement of Breast Cancer Detection Using Dual-Layer Spectral CT," *Diagnostics*, vol. 14, no. 14, Art. no. 14, Jan. 2024, doi: 10.3390/diagnostics14141560.

[17] K. D. Kurz, G. Ringstad, A. Odland, R. Advani, E. Farbu, and M. W. Kurz, "Radiological imaging in acute ischaemic stroke," *Eur. J. Neurol.*, vol. 23, no. S1, pp. 8–17, 2016, doi: 10.1111/ene.12849.

[18] X. Ma, M. Figl, E. Unger, M. Buschmann, and P. Homolka, "X-ray attenuation of bone, soft and adipose tissue in CT from 70 to 140 kV and comparison with 3D printable additive manufacturing materials," *Sci. Rep.*, vol. 12, no. 1, p. 14580, Aug. 2022, doi: 10.1038/s41598-022-18741-4.

[19] K. Suzuki *et al.*, "Quantitative accuracy of computed tomography perfusion under low-dose conditions, measured using a hollow-fiber phantom," *Jpn. J. Radiol.*, vol. 35, no. 7, pp. 373–380, July 2017, doi: 10.1007/s11604-017-0642-y.

[20] G. Y. Cho, S. Kim, J. H. Jensen, P. Storey, D. K. Sodickson, and E. E. Sigmund, "A versatile flow phantom for intravoxel incoherent motion MRI," *Magn. Reson. Med.*, vol. 67, no. 6, pp. 1710–1720, 2012, doi: 10.1002/mrm.23193.

[21] N. Ohno *et al.*, "Technical Note: Development of a cranial phantom for assessing perfusion, diffusion, and biomechanics," *Med. Phys.*, vol. 44, no. 5, pp. 1646–1654, 2017, doi: 10.1002/mp.12182.

[22] J.-W. Chai *et al.*, "Spoiled gradient-echo as an arterial spin tagging technique for quick evaluation of local perfusion," *J. Magn. Reson. Imaging*, vol. 16, no. 1, pp. 51–59, 2002, doi: 10.1002/jmri.10128.

[23] Y. Wang *et al.*, "A 3D-printed phantom for quality-controlled reproducibility measurements of arterial spin labeled perfusion," *Magn. Reson. Med.*, vol. 91, no. 2, pp. 819–827, 2024, doi: 10.1002/mrm.29886.

[24] T. C. Potdevin, J. B. Fowlkes, A. P. Moskalik, and P. L. Carson, "Analysis of refill curve shape in ultrasound contrast agent studies," *Med. Phys.*, vol. 31, no. 3, pp. 623–632, 2004, doi: 10.1118/1.1649534.

[25] J. H. Lee *et al.*, "Perfusion Assessment Using Intravoxel Incoherent Motion-Based Analysis of Diffusion-Weighted Magnetic Resonance Imaging: Validation Through Phantom Experiments," *Invest. Radiol.*, vol. 51, no. 8, p. 520, Aug. 2016, doi: 10.1097/RLI.0000000000000262.

[26] M. E. Kamphuis *et al.*, "Development of a dynamic myocardial perfusion phantom model for tracer kinetic measurements," *EJNMMI Phys.*, vol. 9, no. 1, p. 31, Apr. 2022, doi: 10.1186/s40658-022-00458-y.

[27] R. R. Eikholt, "Towards the Quantification of Fluorescence Angiography for Perfusion Assessment," Enschede, May 2025. [Online]. Available: https://purl.utwente.nl/essays/106324

[28] M. Ressner, L.-A. Brodin, T. Jansson, L. Hoff, P. Ask, and B. Janerot-Sjoberg, "Effects of Ultrasound Contrast Agents on Doppler Tissue Velocity Estimation," *J. Am. Soc. Echocardiogr.*, vol. 19, no. 2, pp. 154–164, Feb. 2006, doi: 10.1016/j.echo.2005.09.025.

[29] E.-J. Kim, D.-H. Kim, S. H. Lee, Y.-M. Huh, H.-T. Song, and J.-S. Suh, "Simultaneous acquisition of perfusion and permeability from corrected relaxation rates with dynamic susceptibility contrast dual gradient echo," *Magn. Reson. Imaging*, vol. 22, no. 3, pp. 307–314, Apr. 2004, doi: 10.1016/j.mri.2004.01.012.

[30] M. S. Sarwar, A. Vallatos, C. H. Lau, A. Waldman, S. Dimartino, and M. J. Thrippleton, "3D-printable phantoms for quantitative dynamic contrast-enhanced MRI," *Magn. Reson. Med.*, vol. n/a, no. n/a, doi: 10.1002/mrm.30595.

[31] M. K. George *et al.*, "Perfusion flow phantoms with randomly oriented microchannels," in *Medical Imaging 2018: Ultrasonic Imaging and Tomography*, SPIE, Mar. 2018, pp. 7–13. doi: 10.1117/12.2296803.

[32] D. Ng, H. N. Nikolov, E. Tai, D. Gelman, D. W. Holdsworth, and M. Drangova, "Modular 3D-printed liver tumour phantom for modelling embolization procedures," in *Medical Imaging 2024: Image-Guided Procedures, Robotic Interventions, and Modeling*, SPIE, Mar. 2024, pp. 304–311. doi: 10.1117/12.3004837.

[33] B. Ebrahimi, S. D. Swanson, and T. E. Chupp, "A Microfabricated Phantom for Quantitative MR Perfusion Measurements: Validation of Singular Value Decomposition Deconvolution Method," *IEEE Trans. Biomed. Eng.*, vol. 57, no. 11, pp. 2730–2736, Nov. 2010, doi: 10.1109/TBME.2010.2055866.

[34] L. Goris, S. Gouma, J. J. Pautasso, K. Michielsen, and I. Sechopoulos, "Modular breast and tumor perfusion phantoms for validation of 4D dynamic contrast-enhanced dedicated breast CT," in *Medical Imaging 2025: Physics of Medical Imaging*, SPIE, Apr. 2025, pp. 154–160. doi: 10.1117/12.3048919.

[35] B. Driscoll, H. Keller, and C. Coolens, "Development of a dynamic flow imaging phantom for dynamic contrast-enhanced CT," *Med. Phys.*, vol. 38, no. 8, pp. 4866–4880, 2011, doi: 10.1118/1.3615058.

[36] A. J. Allphin, D. P. Clark, C. J. Gil, M. L. Tomov, V. Serpooshan, and C. T. Badea, "Advancing preclinical micro-photon counting CT perfusion imaging: from phantom experiments to in vivo applications," Accessed: Aug. 13, 2025. [Online]. Available: https://www.spiedigitallibrary.org/conference-proceedings-of-spie/12925/129250J/Advancing-preclinical-micro-photon-counting-CT-perfusion-imaging--from/10.1117/12.3006836.full

[37] V. Filippou and C. Tsoumpas, "Recent advances on the development of phantoms using 3D printing for imaging with CT, MRI, PET, SPECT, and ultrasound," *Med. Phys.*, vol. 45, no. 9, pp. e740–e760, Sept. 2018, doi: 10.1002/mp.13058.

[38] *Additive manufacturing - General principles - Fundamentals and vocabulary:* doi: 10.3403/30448424.

[39] S. C. Ligon, R. Liska, J. Stampfl, M. Gurr, and R. Mülhaupt, "Polymers for 3D Printing and Customized Additive Manufacturing," *Chem. Rev.*, vol. 117, no. 15, pp. 10212–10290, Aug. 2017, doi: 10.1021/acs.chemrev.7b00074.

[40] F. Okkalidis *et al.*, "Characterization of Commercial and Custom-Made Printing Filament Materials for Computed Tomography Imaging of Radiological Phantoms," *Technologies*, vol. 12, no. 8, p. 139, Aug. 2024, doi: 10.3390/technologies12080139.

[41] F. Zhang *et al.*, "The recent development of vat photopolymerization: A review," *Addit. Manuf.*, vol. 48, p. 102423, Dec. 2021, doi: 10.1016/j.addma.2021.102423.

[42] F. Labs, "The Complete Guide to Watertight 3D Printing | Forge Labs." Accessed: Nov. 02, 2025. [Online]. Available: https://forgelabs.com/blog/watertight-3d-printing-comprehensive-guide

[43] G. G. Kailo *et al.*, "Food safety-based evaluation of 3D printed objects," *Analecta Tech. Szeged.*, vol. 17, no. 4, pp. 1–9, Nov. 2023, doi: 10.14232/analecta.2023.4.1-9.

[44] A. J. Aschoff, C. Catalano, M. A. Kirchin, M. Krix, and T. Albrecht, "Low radiation dose in computed tomography: the role of iodine," *Br. J. Radiol.*, vol. 90, no. 1076, p. 20170079, doi: 10.1259/bjr.20170079.

[45] S. S. H. Burmester, C. D. Rielly, and M. F. Edwards, "The Mixing of Miscible Liquids with Large Differences in Density and Viscosity," in *Fluid Mechanics of Mixing*, vol. 10, R. King, Ed., in Fluid Mechanics and Its Applications, vol. 10. , Dordrecht: Springer Netherlands, 1992, pp. 83–90. doi: 10.1007/978-94-015-7973-5_10.

[46] Bracco, "Iomeron." [Online]. Available: ch-en-2020-08-24-spc-iomeron.pdf

[47] E. Nader *et al.*, "Blood Rheology: Key Parameters, Impact on Blood Flow, Role in Sickle Cell Disease and Effects of Exercise," *Front. Physiol.*, vol. 10, p. 1329, Oct. 2019, doi: 10.3389/fphys.2019.01329.

[48] A. Volk and C. J. Kähler, "Density model for aqueous glycerol solutions," vol. 59, pp. 75–75, 2018, doi: 10.1007/s00348-018-2527-y.

[49] L. Kleimeier, L. Goris, L. Oostveen, W. Klein, and I. Sechopoulos, "Optimizing CT lymphangiography: insights from fluid dynamics." Zenodo. [Online]. Available: https://doi.org/10.5281/zenodo.17494908

[50] M. Kamphuis, "Quantitative myocardial perfusion imaging : a novel multimodality validation phantom," PhD, University of Twente, Enschede, The Netherlands, 2022. doi: 10.3990/1.9789036553780.

Contacts of the corresponding author:

Author:	Ioannis Sechopoulos
Institute:	Radboud University Medical Centre, Department of Medical Imaging
Street:	Geert Grooteplein 10
City:	Nijmegen
Country:	The Netherlands
Email:	Ioannis.Sechopoulos@radboudumc.nl